Science and Technology of Lithium Batteries – Kluwer Academic Publishers (2003)

Chapter 16

UNDERSTANDING PHASE TRANSFORMATIONS IN LITHIUM BATTERY MATERIALS BY TRANSMISSION ELECTRON MICROSCOPY

Y. Shao-Horn

Massachusetts Institute of Technology
Cambridge, Massachusetts 02139

16.1. INTRODUCTION

Downsizing of electronic components demands energy storage systems with high energy and power densities, and thus continuously drives battery research and development efforts. The most commonly used batteries in portable computers and cellular phones are lithium rechargeable batteries[1]. In these batteries, chemical energy stored in the positive electrode is released and converted into electrical energy during discharge through an intercalation (insertion) process by which lithium ions are incorporated within the host structure of the positive electrode material. During charge, the process is reversed (de-intercalation) and electrical energy is applied to remove lithium ions from the positive electrode. Lithium transition metal oxides that host mobile lithium ions on the interstitial sites have been studied as positive electrode materials and the intercalation and de-intercalation processes of lithium ions are accompanied by redox of transition metal ions. The energy output of lithium rechargeable batteries is dependent on the voltage upon which lithium ions are inserted and the number of interstitial sites that can accommodate lithium ions in the host structure. Ideally, intercalation and de-intercalation of lithium ions and redox of transition metal ions, should leave the host structure intact. In practice, however, variation in lithium content in the host structure leads to lattice expansion or contraction, migration of transition metal ions and local or global lattice distortion as a result of ordering of lithium and vacancies or Jahn-Teller distortion of transition metal ions. These structural changes can 1) induce stresses and strains within lithium transition metal oxide crystals, 2) affect the electronic conductivities of lithium battery materials, and 3) lead to irreversible phase changes and thus decrease in energy outputs of lithium batteries. Therefore, much research has been focused on characterizing structural changes of lithium transition metal

oxides associated with lithium intercalation and de-intercalation, and modifying material chemistry to suppress phase transformations and to optimize lithium battery performance.

Layered O3 Li_xCoO_2[2-4], Li_xNiO_2[5-8] and Li_xMnO_2[9-11], spinel $Li_xMn_2O_4$[12-14] and olivine Li_xFePO_4[15] are the most studied positive electrode materials in the last two decades[16,17]. Layered Li_xCoO_2 and Li_xNiO_2 are stable upon lithium intercalation or de-intercalation despite the fact that several phase transformations are observed from lithium composition $x = 1$ to $x = 0$. Of significance, lithium and vacancy ordering[3], Jahn-Teller induced[18], and metal-insulator[19] transformations have been reported. On the other hand, layered Li_xMnO_2 host structure is not stable upon lithium intercalation or de-intercalation and transforms to a spinel-related structure[20-22]. Spinel $Li_xMn_2O_4$ structure is stable upon electrochemical cycling but can undergo many interesting phase transformations induced by Jahn-Teller distortion[13] or charge ordering[23-25]. Extensive research efforts have focused on understanding the structural changes underwent in these lithium transition metal oxides and their effects on lithium battery performance.

Conventional bulk analytical techniques, such as X-ray and neutron powder diffraction and electrochemical characterization, are used routinely to provide overall, averaged chemical and structural information on lithium battery electrodes. Although the bulk diffraction techniques enable accurate determination of distances and angles of atoms in the volume-averaged crystal structures, they are insensitive to spatially localized phase transformations and ordering transitions of lithium and vacancies or charges in lithium electrode materials. In particular, Garcia-Adeva *et al.* have recently pointed out the ambiguities in revealing nanoscale heterogeneity or aperiodic phase separation by conventional powder diffraction techniques[26]. Electrochemical methods, such as lithium cell voltage monitoring, are very sensitive to changes of local environments available for lithium ions at the electrode-electrolyte interface but provide little information on the details of structural features responsible for the electrochemical responses. Therefore, bulk analytical techniques alone are inadequate to identify critical material features and phase transformations in lithium electrode materials that limit battery performance. Combination of transmission electron microscopy (TEM) analyses, bulk diffraction and electrochemical techniques has proven invaluable in this regard. TEM and associated techniques enable microstructural characterization of lithium battery materials from both local structural and chemistry points of view.

Although TEM techniques have been used extensively in materials science, solid state chemistry and mineral science[27-30], application of these techniques in lithium battery research has been comparatively recent[21,31-52]. TEM techniques provide high-spatial resolution single-crystal diffraction information from individual lithium transition metal oxide crystals complementary to X-ray and neutron powder diffraction as electrons can be

focused easily. In addition, one can use TEM imaging to detect the phase distribution in the electrode that provides valuable insights to heterogeneous phase transformation mechanisms, and imperfections in the lithium transition metal oxide crystals, which are introduced either during material synthesis or electrochemical cycling. Moreover, high-resolution TEM imaging and image simulation can permit direct visualization of atomic arrangements and modifications associated with structural defects and modifications, as demonstrated by imaging stacking faults in orthorhombic $LiMnO_2$[48] and the imaging of lithium ions in $LiCoO_2$[39]. Furthermore, recent electron energy loss spectroscopy (EELS) studies have provided evidence for charge compensation mechanisms in Li_xCoO_2[51] and $Li_xNi_{0.8}Co_{0.2}O_2$[49], and transition metal clustering in $LiNi_{1-x}Al_xO_2$[53]. Therefore, combining bulk analytical studies with TEM studies has led to significant advances in identifying phase transformation mechanisms of lithium electrode materials, understanding of structure-property relationships, and providing direction in the design of new battery materials.

In this chapter, we focus on understanding phase transformations of O3 and O2 layered Li_xCoO_2, O3 Li_xNiO_2, O3 Li_xMnO_2 and spinel $Li_x[Mn]_2O_4$ underwent during electrochemical cycling or upon materials synthesis. Much of our information is derived from electron diffraction data obtained in the transmission electron microscope (TEM). We begin with an overview of commonly used TEM techniques. We then illustrate how TEM techniques can be used to reveal and understand electrochemically induced phase transformations in lithium electrode materials and understand their effects on the electrochemical performance of lithium batteries. Electron diffraction has provided the first experimental evidence for order-disorder phenomena of lithium and vacancy in O3 and O2 derived Li_xCoO_2 and O3 derived Li_xNiO_2. In addition, high spatial resolution of TEM techniques is powerful in identifying localized phase transitions such as revealing the presence of tetragonal, Jahn-Teller distorted $Li_2[Mn_2]O_4$ in $Li_x[Mn_2]O_4$ electrodes discharged to 3.0 V and above, which supports one of previously proposed hypotheses responsible for capacity degradation of 4 V $Li_x[Mn_2]O_4$ electrodes during electrochemical cycling. Moreover, electron diffraction has revealed and quantified intermediate cation configurations between the spinel and the layered configurations in as-prepared low-temperature $LiCoO_2$ (LT-$LiCoO_2$) and cycled layered O3 Li_xMnO_2 electrodes, which leads to electrochemical properties of LT-Li_xCoO_2 and Li_xMnO_2 electrodes significantly different from layered O3 Li_xCoO_2. A rapid, irreversible phase transformation from the layered to a spinel-related structure in cycled Li_xMnO_2 electrodes leads to significant modification in the electrochemical voltage profile and reduction in reversible capacity, which limits the commercialization of layered Li_xMnO_2 in lithium batteries. In all these cases, TEM techniques identify critical phase

transformations in lithium transition metal oxides that control the electrochemical performance of lithium batteries.

16.2. TRANSMISSION ELECTRON MICROSCOPY

Electron diffraction and TEM imaging are effective in probing localized structural modifications in lithium electrode materials on the nanometer-scale.

16.2.1. Electron Diffraction of Crystals

Kinematical theory that assumes that the electron beam is scattered weakly by the material (the amplitude of the scattered electron wave is much less than the incident electron wave) is used here. We begin with scattering of electrons from atoms. The wave function ψ of the electron at non-relativistic velocities satisfies the time independent Schrodinger equation, for stationary states:

$$\frac{\boldsymbol{h}^2}{8\pi^2 \boldsymbol{m}_0 \boldsymbol{e}} \nabla^2\psi + (\boldsymbol{E} + \boldsymbol{V})\psi = 0 \qquad (1)$$

Where $\boldsymbol{eE}$ is the total energy of the electron and $-\boldsymbol{eV}$ is the potential energy. Within the kinematical approximation, the amplitude of the wave scattered from an atom at a point P (at $\boldsymbol{r}$ from the origin) can be expressed by:

$$\psi_s = \frac{2\pi \boldsymbol{m}_0 \boldsymbol{e}}{\boldsymbol{h}^2} \frac{\exp(2\pi i \boldsymbol{k} \boldsymbol{r}_i)}{\boldsymbol{r}} \int_{atom} \boldsymbol{V}(\boldsymbol{r}_i) \exp(2\pi i \boldsymbol{K}' \boldsymbol{r}_i) d\tau_i \qquad (2)$$

where $\boldsymbol{V}(\boldsymbol{r}_i)$ is the atomic potential at a point $\boldsymbol{r}_i$, $\boldsymbol{k}$ is the wave vector and $\boldsymbol{K'} = \boldsymbol{k}'-\boldsymbol{k}$. Using the Born approximation, we obtain the atomic scattering amplitude for electrons:

$$\boldsymbol{f}_{electrons}(\theta) = \frac{\boldsymbol{m}_0 \boldsymbol{e}^2}{2\boldsymbol{h}^2} \left(\frac{\lambda}{\sin\theta} \right)^2 (\boldsymbol{Z} - \boldsymbol{f}_x) \qquad (3)$$

where $\boldsymbol{f}_x$ is the atomic scattering factor for X-rays and $\boldsymbol{Z}$ is the atomic number. The interaction between the atom and electrons consists of scattering from both the nucleus and electron cloud. This is different from X-ray diffraction, which interacts with atomic electrons and the atomic scattering amplitude for X-rays can be expressed by:

$$\boldsymbol{f}_{x-rays}(\theta) = \frac{\boldsymbol{e}^2}{\boldsymbol{m}_0 \boldsymbol{c}^2} \boldsymbol{f}_x \qquad (4)$$

As shown in Equations 3 and 4, the scattering power of atoms for electrons is much greater than for X-rays. In addition, the atomic scattering factors for electrons increase smoothly with atomic number, except at low scattering angles, but not as quickly as X-rays. Therefore, electron diffraction is more sensitive in detecting light atomic number elements than X-ray diffraction. It should be noted that the electron scattering factor of lithium relative to transition metals is significantly larger than that of X-rays as a result of strong interactions between electrons and atoms, as shown in Figure 16.1.. Therefore, electron diffraction can be used to probe the presence of superstructures induced by ordering of light elements or charges, which has typically proven difficult for X-ray or neutron powder diffraction.

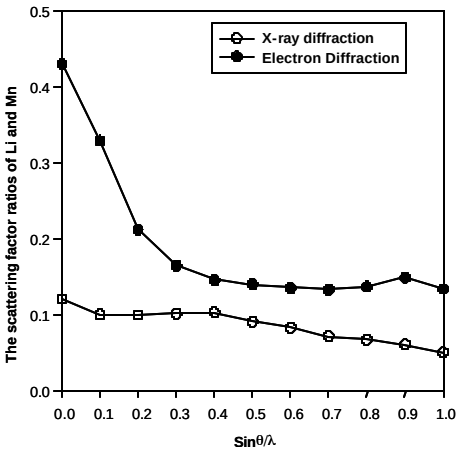

Figure 16.1. The ratios between the X-ray and electron scattering factors of lithium to manganese atoms (f_{Li}/f_{Mn}) as a function of Sinθ/λ? Note that the ratio, $f_{Li}/f_{Mn,}$ for electron diffraction is considerably larger than that of X-ray diffraction.

The scattered electron wave from one crystal can be described by:

$$\psi_s = \frac{\exp(2\pi i \mathbf{k} \mathbf{r}_i)}{r} \sum_i^N f_i(\theta) \exp\left(-2\pi i \mathbf{K}' \cdot \mathbf{r}_i\right) \qquad (5)$$

where $f_i(\theta)$ is the atomic electron scattering factor of site i in the crystal. The absolute intensity of the scattered wave can be obtained by taking the product of the wave function with its complex conjugate.

Electron diffraction patterns of a powder sample can be obtained by selected area electron diffraction from regions as small as 0.5 μm or by nanodiffraction or convergent beam electron diffraction, in which a focused electron beam is used to obtain diffraction patterns from regions down to 1 nm. Single-crystal electron diffraction data obtained from lithium transition metal oxide crystals can be viewed as planes in its reciprocal space, which

consists of the transmitted electron beam and individual diffraction spots. Detailed procedures on electron diffraction pattern indexing can be found in the TEM textbook by Fultz and Howe[29]. Because of strong dynamic diffraction effects in electron diffraction of most crystals, electron diffraction intensities are often used qualitatively, and quantitative analysis of electron diffraction intensities is less reliable than X-ray or neutron diffraction.

16.2.2. TEM Imaging

Diffraction contrast in TEM images results from variation in the diffracted intensity from the material. Bright-field images (the transmitted beam intensity) and dark-field images (the diffracted beam intensity) provide information about microstructural features of materials. Imperfections such as dislocations, stacking faults, domain and phase boundaries within the crystal displace the unit cell and thus introduce a phase change in the scattered wave, which leads to intensity variation in both dark-field and bright field images. Dark-field imaging has been particularly useful for studying domain structures within lithium transition metal oxide crystals induced by lithium intercalation or de-intercalation.

In addition to diffraction contrast, imaging of lattice fringes has been commonly used in studying phase transformations in lithium battery materials on the nanometer scale. The intensity distribution of the incident beam and one diffracted beam gives a modulation with the spacing of the plane being diffracted for a given crystal orientation and thickness, which reveals the lattice of the lithium electrode material in the form of sine fringes as shown as follows:

$$I = 1 + R^2 - 2R\sin\left(\frac{2\pi x}{d} - s_0\right) \qquad (6)$$

Where d is the spacing of the plane being diffracted, x is the direction of modulation in the image, and R and s_0 are constants for a given thickness and crystal orientation). It should be noted that the positions of the lattice fringes bear no apparent relation to the position of atomic planes. Further detailed information on lattice image formation can be found in TEM textbooks[27,30].

16.2.3. TEM Sample Preparation

The requirements of a good TEM sample include 1) electron beam transparency, which limits maximum thickness to 5 μm, and 2) a clean surface (free of contaminants). Lithium transition metal oxides used in lithium batteries are typically in the form of powders and the crystal sizes are dependent on synthesis routes, usually in the range of 20 nm to 10 μm. TEM samples of these oxides can be obtained from the following preparation

procedure: 1) grind the powder in agate mortar and pestle, 2) suspend the powder in an organic solvent in an ultrasonic bath, 3) deposit suspended particles onto a TEM copper grid coated with lacey carbon. If crystal sizes of lithium electrode materials are significantly greater than 1 μm, mechanical thinning of these crystals is needed. Microtoming is an effective method to produce thin TEM sections of as-prepared lithium transition metal oxides. The material is first embedded in epoxy resin. Ultrathin sections on the order of 60 nm cut with diamond knives using an ultramicrotome are floated on water and then transferred to TEM copper grids with lacey carbon support.

16.2.4. Caveats to TEM Techniques

Although electron diffraction and TEM imaging techniques are powerful in probing localized structural defects and phase transitions, they have a few limitations in comparison to bulk analytic techniques. Three of the most important are 1) the sampling statistics is very poor, 2) only crystals with thickness less than 1μm can be analyzed and 3) kinematical theory is only qualitative. Therefore, in order to ensure the fact that crystals analyzed in the TEM are representative of the bulk materials, it is necessary to combine TEM results with bulk analytical information including X-ray powder diffraction and electrochemical data. In addition, there are concerns with regard to the stability of materials during TEM sample preparation and under the electron beam. This is a serious issue when studying highly de-intercalated lithium battery materials in the TEM. Performing TEM data collection at liquid nitrogen temperature can remove some materials instability problems related to thermal breakdown under the electron beam.

16.3. LITHIUM AND VACANCY ORDERING

Ordering of lithium and vacancy has been first proposed in intercalation compounds of layered chalcogenides such as Li_xTiS_2[54] and Li_xTaS_2[55]. At room temperature, lithium ions that reside in octahedral sites are mobile. Lithium ions are constrained to occupy certain sites preferentially as a result of long-range, repulsive, Coulombic interactions among lithium ions, which lead to formation of superlattices at various lithium contents parallel to the transition metal layers. Although direct observation of lithium ordering by X-ray diffraction is difficult, characteristic peaks in the incremental capacity dx/dV vs. x plots are observed at specific lithium compositions where ordering is expected in Li_xTiS_2[54]. As a similar electrochemical feature is noted in Li/Li_xCoO_2 cells where x is near 0.5, Reimers and Dahn[3] have proposed lithium and vacancy ordering in $Li_{0.5}CoO_2$ obtained from lithium de-intercalation of layered O3 $LiCoO_2$. The first direct experimental evidence of lithium ordering is the observation of superstructures in the electron

diffraction patterns of layered Li_xNiO_2[42,56]. Subsequently electron diffraction and TEM imaging have successfully revealed order-disorder phenomena of lithium and vacancy in layered O3-$Li_{0.5}CoO_2$[37] and O2-Li_xCoO_2[38] electrode materials. Moreover, first-principles studies support the concept of lithium and vacancy ordering in these layered compounds[57-64]. Van der Ven and Ceder have shown that lithium ordering reduces lithium ion mobility as evidenced by a two-order of magnitude reduction in the chemical diffusion coefficient in Li_xCoO_2 at ordered compositions[57]. Lithium and vacancy ordering can be suppressed by metal substitution in the transition metal layers[65,66], which eliminates phase transformations and greatly affects electrochemical cycling of lithium batteries. Therefore, understanding order-disorder phenomena of lithium and vacancy in lithium battery materials is not only essential to further improve the cycling performance of lithium rechargeable batteries but also important to provide new insights to lithium-lithium interactions in these transition metal oxides and their impact on kinetic properties and to design of better lithium electrode materials. In this section, we focus on understanding order-disorder transformations of lithium and vacancy in these layered materials by electron diffraction.

16.3.1. Lithium and Vacancy Ordering in O3 Li_xNiO_2

O3 layered $LiNiO_2$ consists of lithium and nickel sheets stacked alternatively in-between AB CA BC AB close-packed oxygen arrays. The structure is typically defined in a hexagonal cell that has a trigonal symmetry with space group $R\bar{3}m$. Lithium de-intercalation from $LiNiO_2$ leads to many phase transformations that occur as a function of lithium concentration[67-69]. Electron diffraction of Li_xNiO_2 has lent first experimental evidence of lithium and vacancy ordering in lithium transition metal oxides at various lithium concentrations, x = 0.25, 0.33 and 0.65, as shown in Figure 16.2.[42,56]. It should be noted that at lithium compositions of x = 0.25 and x = 0.33, order-disorder of lithium and vacancy is associated with noticeable inflexion points in the voltage profile of Li/Li_xNiO_2 cells, similar to lithium ordering in Li_xTiS_2[54]. However, lithium ordering in Li_xNiO_2 near x = 0.65 is different and no pronounced modification in the voltage profile is associated with this ordering transformation. X-ray powder diffraction studies[42,67-69] of Li_xNiO_2 show that this composition falls in the wide monoclinic, single-phase region with lithium composition in the range of $0.5 \leq x \leq 0.75$. The stability of the monoclinic phase, important to electrochemical performance, has been a subject of debate.

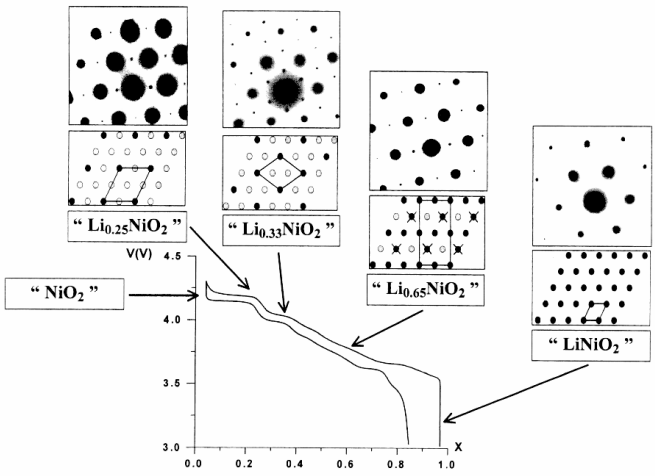

Figure 16.2. The voltage profile of Li_xNiO_2 vs. lithium as a function of lithium content x from Delmas *et al.*[56]. Note that the electron diffraction patterns obtained from various points in the voltage profile show different superstructures, which is not visible in the X-ray powder diffraction patterns of Li_xNiO_2 samples.

It has been proposed that this symmetry reduction to monoclinic is driven and stabilized by either a cooperative Jahn-Teller induced distortion of NiO_2 octahedra[68] or ordering of lithium and vacancy[42]. Using selected area electron diffraction, Peres *et al.* have provided experimental evidence of a 2x2x2 superstructure of ordered lithium and vacancy in the monoclinic phase (not detectable in the X-ray powder diffraction patterns) in a $Li_{0.63}Ni_{1.02}O_2$ sample. This superstructural model can be used to accommodate a range of lithium concentrations, in which lithium ordering stabilizes the monoclinic phase[42]. Recent first-principle studies[64] of layered Li_xNiO_2 have shown that lithium and vacancy ordering is coupled with monoclinicity and weak Jahn-Teller distortion of Ni^{3+} ions in this phase region. In contrast to the 2x2x2 superstructure of the monoclinic cell found by electron diffraction studies[42], different superstructures have been predicted from first-principles studies[63]: one superstructure with 2x1x1 of the monoclinic cell at $Li_{0.75}NiO_2$ and the other with $\sqrt{3}$ x $\sqrt{7}$ x1 of the parent hexagonal cell at $Li_{0.4}NiO_2$. In addition to superstructures in the monoclinic phase region, one $2\sqrt{3}$ x$2\sqrt{3}$ x1 superstructure[63] of the hexagonal cell is found at $Li_{0.5}NiO_2$ via computation, though no experimental evidence of ordering exists for this composition at this time. Discrepancies in the detailed nature of the superstructures of ordered lithium and vacancy in the monoclinic Li_xNiO_2 between first-principles and electron diffraction results require further investigations.

16.3.2. Lithium and Vacancy Ordering in O3 Li_xCoO_2

O3 layered $LiCoO_2$, isostructural to O3 $LiNiO_2$, has become the most commonly used positive electrode material in lithium rechargeable batteries since the concept of reversible lithium removal from and insertion into $LiCoO_2$ was first introduced by Goodenough *et al.*[2]. Intensive research and development efforts have been devoted to understanding the physical properties and phase transformations of Li_xCoO_2 ($0 \le x \le 1$) in order to improve the energy output and cycle life of lithium batteries[3,4,19,44,59,70-76]. Lithium de-intercalation from $LiCoO_2$ leads to several phase transformations, detailed as follows: 1) $0.75 \le x \le 0.94$, a first-order transformation from a rhombohedral insulating $Li_{0.94}CoO_2$ phase to a rhombohedral metallic $Li_{0.75}CoO_2$ phase[3,4,19,73]; 2) $x \approx 0.5$, a phase transformation from the rhombohedral to monoclinic symmetry[3,4], 3) $0.17 < x < 0.33$, a phase transformation from O3 rhombohedral to H1-3[77,78] and 4) $0 < x < 0.12$, a phase transformation from H1-3 to O1[75,77,78]. Of particular interest has been understanding the phase transformation from the rhombohedral to monoclinic symmetry in Li_xCoO_2 at $x \approx 0.5$, which has been attributed to the ordering of lithium ions and vacancies within the layers (in-plane ordering) by X-ray powder diffraction experiments[3] and by first-principle studies[60], as shown in Figure 16.3..

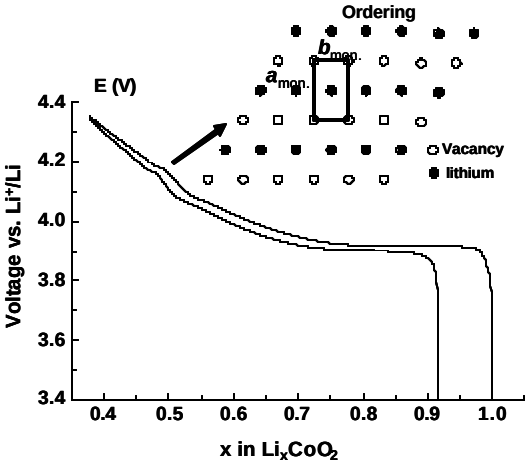

Figure 16.3. Typical voltage profiles of Li/Li_xCoO_2 cells and the inflexion point is correlated with order-disorder of lithium and vacancy in Li_xCoO_2 ($x \approx 0.5$)[3,37].

Experimental electron diffraction analysis[37] of Li_xCoO_2 with $x \approx 0.5$ and electron diffraction simulation of disordered $Li_{0.5}CoO_2$ with space group *C2/m* and ordered $Li_{0.5}CoO_2$ with space group *P2/m* have confirmed the

proposed in-plane lithium ordering. The in-plane ordering along the $[110]_{hex.}$ and equivalent directions allows the formation of mazed crystals, and electron diffraction patterns with appearance that resembles those of the spinel structure can be fully explained by lithium and vacancy ordering and coexistence of two or three variants, as shown in Figure 16.4.[37]. Therefore, it is believed that electron diffraction data[37] do not suggest the layered to spinel transformation in Li_xCoO_2, and the stability of the layered Li_xCoO_2 upon lithium removal is in agreement with the excellent cycling performance of Li/Li_xCoO_2 batteries. In addition to in-plane lithium ordering, evidence of ordering of lithium and vacancy arrangements perpendicular to the ***c*** axis of the hexagonal parent cell is also found, which is consistent with first-principles prediction[78].

We now compare and discuss the difference in lithium ordering arrangements between Li_xNiO_2 and Li_xCoO_2 systems. The number of ordered lithium arrangements found in Li_xNiO_2 obtained from electron diffraction and first-principles is significantly more than Li_xCoO_2. Lithium ordering occurs at Li_xCoO_2 with $x = 0.5$ and $x = 1/3$ where lithium ordering in Li_xNiO_2 has been proposed at $x = 0.25$, 0.4, 1/3, 0.5, 0.6 and 0.75[42,63]. In theory, in-plane ordering of lithium and vacancy should lead to deviation in the *a/b* ratio of the rhombohedral layered structure as the electrostatic interactions of lithium ions along the *a* and *b* directions are different. The deviation in the *a/b* ratio from the ideal value (1.732) decreases the crystal symmetry from rhombohedral to monoclinic, where the crystal structure can be modified by varying the *a/b* ratio and/or β. It is interesting to note that the structural changes associated with lithium ordering at the $Li_{0.5}CoO_2$ composition and in the Li_xNiO_2 ($0.50 \le x \le 0.75$) system are different. Changes in the *a/b* ratio would considerably modify the cobalt-oxygen bonds and distort the CoO_6 octahedra, in Figure 16.13., image simulation via the "weak-phase object" approximation indicates that resolutions higher than 1 Å are needed to resolve individual lithium ions in layered CoO2 matrix DDIN EN.CITE <EndNote><Cite><Autho different β (107.89°) value from the rhombohedral symmetry upon lithium and vacancy ordering. In contrast, the Li_xNiO_2 ($0.50 \le x \le 0.75$) structure has a small change in β (109.75°) but a large increase in the *a/b* ratio (1.764) as Jahn-Teller distorted Ni^{3+} ions can accommodate the distortion in the *a* and *b* direction upon lithium and vacancy ordering.

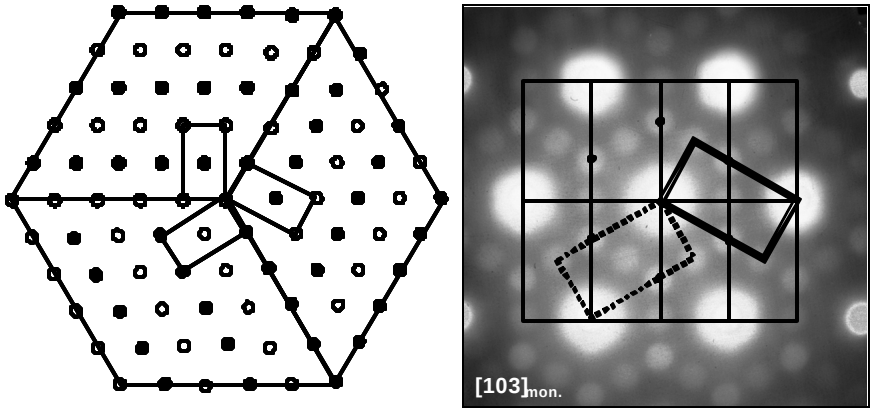

Figure 16.4. Left, three possible orientations for lithium and vacancy ordering in the lithium layers and the monoclinic unit cell of $Li_{0.5}CoO_2$ and right, an experimental diffraction pattern along the $[103]_{mon.}$ zone axis of the monoclinic unit cell or the $[001]_{hex.}$ zone axis of the hexagonal unit cell, which revealed the reflections associated with lithium and vacancy ordering from all three variants[37].

16.3.3. Lithium Ordering in O2 derived Li_xCoO_2

Layered O2 $LiCoO_2$ with a unique AB CB AB oxygen packing, first reported by Delmas *et al.*[79], is metastable to layered O3 $LiCoO_2$ with O3-type AB CA BC oxygen packing. Recently O2 $LiMO_2$ (M = Ni, Mn, Co, etc.) compounds have been reinvestigated for lithium rechargeable battery applications[80-89] as their structural derivatives upon lithium de-intercalation and intercalation are stable with respect to the spinel-related framework. Lithium removal from O2-$LiCoO_2$ leads to the formation of various novel phases as shown by X-ray powder diffraction, $T^{\#}2$, $T^{\#}2$' and O6, which are closely related to the O2 crystal structure[82,86,90], as shown in Figure 16.5.. Of particular interest is the $T^{\#}2$-Li_xCoO_2 phase that is stable over a large compositional range ($0.52 < x \leq 0.72$). The stability of this structure is not clearly understood. The $T^{\#}2$ structure has an orthorhombic unit cell and space group *Cmca*, for instance, '$Li_{0.61}CoO_2$' with $a_{orth.}$ = 2.8097 Å, $b_{orth.}$ = 4.8500 Å, and $c_{orth.}$ = 9.9082 Å[82]. Previous studies[87] have reported that lithium ions are located on the 8e type tetrahedral sites in the $T^{\#}2$ structure, where two 8e sites are available per cobalt ion and fewer than half of the 8e sites are occupied by lithium ions. As simultaneous occupancy of adjacent 8e sites is unlikely due to small site-to-site distances (1.4 Å and 2.4 Å), lithium ordering on the 8e sites is expected in the $T^{\#}2$ structure. Nevertheless, it should be noted that the voltage-capacity profile for the entire $T^{\#}2$ compositional range is relatively smooth (Figure 16.5.). The absence of

inflexion points in the voltage profile is significantly different from lithium and vacancy ordering at specific lithium compositions in O3-Li_xNiO_2 and O3-Li_xCoO_2 systems (such as x = 0.25 and 0.33 in Figure 16.2. and x = 0.5 in Figure 16.3.), where pronounced modification in the lithium intercalation voltage is noted.

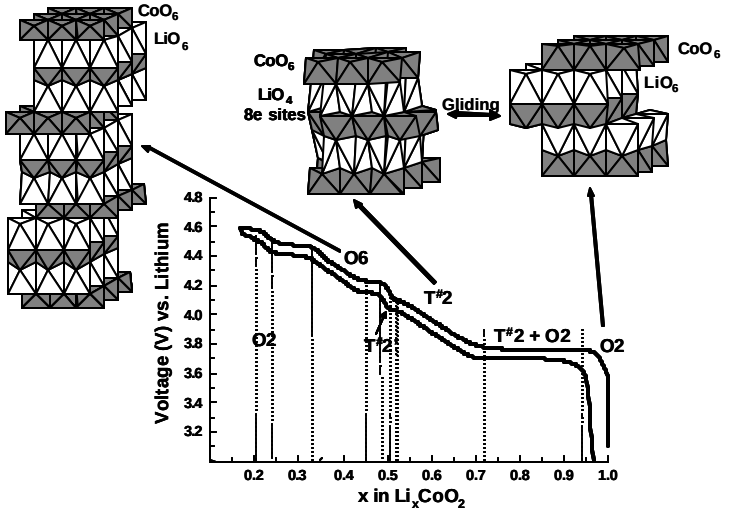

Figure 16.5. Typical galvanostatic charge and discharge voltage profiles of Li/O2-Li_xCoO_2 cells and schematics of the O2-$LiCoO_2$ structure with both lithium and cobalt ions on the octahedral sites, the $T^{\#}2$-Li_xCoO_2 structure with cobalt ions on the octahedral sites and lithium on the 8e tetrahedral sites and the O6-Li_xCoO_2 structure with both lithium and cobalt ions on the octahedral sites[38].

Although no superlattice reflection is found in X-ray and neutron powder diffraction patterns of the $T^{\#}2$ phase, electron diffraction has revealed evidence of several commensurate and incommensurate superstructures in the $T^{\#}2$ phase[38]. A $2a_{orth.}$ x $2b_{orth.}$ x $2c_{orth.}$, a $2a_{orth.}$ x $b_{orth.}$ x $c_{orth.}$ and incommensurate with $q = \gamma a^*_{orth.}$ ($\gamma = 0.23$ and 0.36) superstructures have been identified, which can be explained by different lithium and vacancy ordering configurations. For instance, super reflections present half way between the diffraction center and the fundamental reflections in the $[51\,\bar{2}]_{orth.}$ and the $[02\,\bar{1}]_{orth.}$ diffraction patterns collected from a ''$Li_{0.7}CoO_2$' sample reveal the presence of the $2a_{orth.}$ x $2b_{orth.}$ x $2c_{orth.}$ superstructure and one lithium ordering scheme is proposed to explain this superstructure, as shown in Figure 16.6[38].

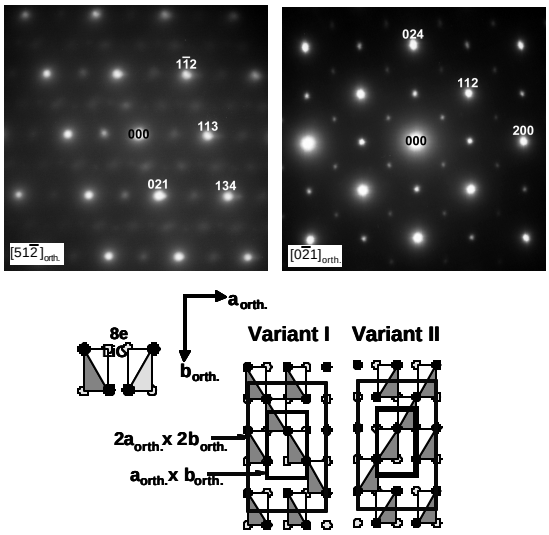

Figure 16.6. The $[51\,\bar{2}\,]_{orth.}$ and the $[02\,\bar{1}\,]_{orth.}$ diffraction patterns collected from the ''$Li_{0.7}CoO_2$' sample reveal the presence of the $2a_{orth.} \times 2\,b_{orth.} \times 2\,c_{orth.}$ superstructure, in which only fundamental reflections are indexed. Lithium and vacancy ordering configurations needed to describe the doubling of the $a_{orth.}$ and $b_{orth.}$ cell parameters are presented. Note that two variants are allowed as two possible orientations exist for the 8e LiO_4 tetrahedra. The doubling of the $c_{orth.}$ cell parameter results from the alternation of these variants in the interslab space along the $c_{orth.}$ axis[38].

In addition to commensurate superstructures, incommensurate periodicities, $q = 0.36 \cdot a^*_{orth.}$ and $0.23 \cdot a^*_{orth.}$, are found in the $[0\,\bar{1}\,1]_{orth.}$ and $[001]_{orth.}$ electron diffraction patterns collected from the '$Li_{0.63}CoO_2$' samples, respectively, as shown in Figure 16.7.[38]. The presence of these incommensurate superstructures suggests that 1) incommensurate lithium and vacancy ordering is preferred to commensurate ordering of lithium and vacancy in large superstructures such as $3a_{orth.} \times b_{orth.} \times c_{orth.}$ and $4a_{orth.} \times b_{orth.} \times c_{orth.}$ and 2) the lithium-lithium interaction can be fairly long range, greater than 10 Å, in the $T^{\#}2$ structure. In addition, it is of significance to point out that the combination of transmission electron microscopy and electron diffraction showed that two or three $T^{\#}2$ variants could coexist in different regions within one $T^{\#}2$ crystal, which led to the development of a domain (mazed) microstructure similar to what has been observed in $Li_{0.5}CoO_2$ (Figure 16.4.).

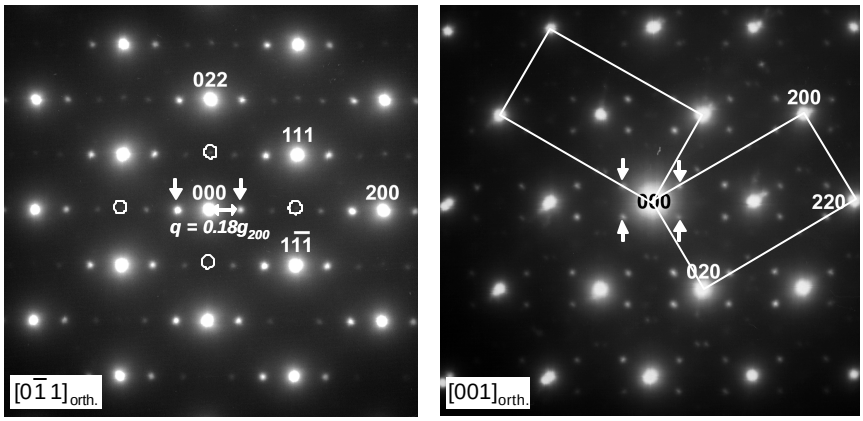

Figure 16.7. The $[0\ \bar{1}\ 1]_{orth.}$ and $[001]_{orth.}$ electron diffraction patterns collected from the '$Li_{0.63}CoO_2$' samples, where the first-order, incommensurate reflections are marked by arrows[38]. Two variants of the incommensurately ordered structure are highlighted in the $[001]_{orth.}$ electron diffraction pattern.

The lack of substantial peaks of ordering transitions within the single-phase $T^{\#}2$-Li_xCoO_2 domain in the differential capacity versus voltage curve could be attributed to the presence of a large number of commensurate and incommensurate superstructures of different chemical compositions with similar Gibbs free energies[38]. The presence of many ordered phases in the $T^{\#}2$ region is supported by a recent first-principles study[62]. It is believed that the presence of various lithium and vacancy ordering configurations improves the stability of the $T^{\#}2$ structure over a range of lithium compositions. Nevertheless, it should be mentioned that the nature of superstructures present and possible lithium ordering configurations in $T^{\#}2$-Li_xCoO_2 were complex and further investigations are needed.

Many fundamental questions with regard to lithium and vacancy ordering in layered intercalation compounds remain to be answered: 1) what are the strain and the stress concentrations in the crystals induced by lithium and vacancy order-disorder transitions and formation of domains, and 2) how do ordering transformations directly affect the cycling of lithium batteries.

16.4. SPATIALLY LOCALIZED PHASE TRANSTIONS

As electrons can be focused much easier than X-rays, the combination of TEM imaging and electron diffraction can provide structural information from regions as small as the probe size of the electron beam, which can be focused down to 5 nm. As electrochemical reactions occur at the interface between the electrode materials and the electrolyte, the performance of

lithium batteries is very sensitive to any phase transformations on the surfaces of electrode materials, in which the secondary phase often cannot be detected by X-ray or neutron powder diffraction due to a low volume fraction in the electrode. TEM techniques have been particularly powerful in detecting new phases formed in lithium intercalation compounds during electrochemical cycling as reported by Thackeray *et al.*[34,40] and Dupont *et al.*[91].

16.4.1 Jahn-Teller Induced Phase Transition in $Li_x[Mn_2]O_4$

$Li/Li_x[Mn_2]O_4$ batteries cycle poorly between 3 and 4 V plateaus, due to the destruction of the spinel framework by a cubic-tetragonal phase transition induced by cooperative Jahn-Teller distortion at 3 V vs. lithium[13]. Gradual loss in capacity is still observed if $Li/Li_x[Mn_2]O_4$ batteries are cycled within the 4 V plateau (the cubic phase domain)[92,93]. It has been proposed that the capacity loss of 4 V $Li/Li_x[Mn_2]O_4$ cells at room temperature is at least partially attributed to the formation of tetragonal $Li_2[Mn_2]O_4$ transformed from cubic $Li[Mn_2]O_4$ at the end of discharge[92]. However, the tetragonal $Li_2[Mn_2]O_4$ phase is not detected by X-ray powder diffraction of the cycled $Li_x[Mn_2]O_4$ electrodes in the 4 V range. If the cubic-tetragonal transition is localized, especially on the surface of crystals, it can considerably affect the reversibility of the lithium intercalation process, even though the volume fraction of the tetragonal phase is insignificant in the $Li_x[Mn_2]O_4$ electrode. Using high-spatial resolution TEM techniques, the presence of localized tetragonal domains at the surface of cubic $Li_x[Mn_2]O_4$ spinel crystals in cycled electrodes [34,40] has been confirmed.

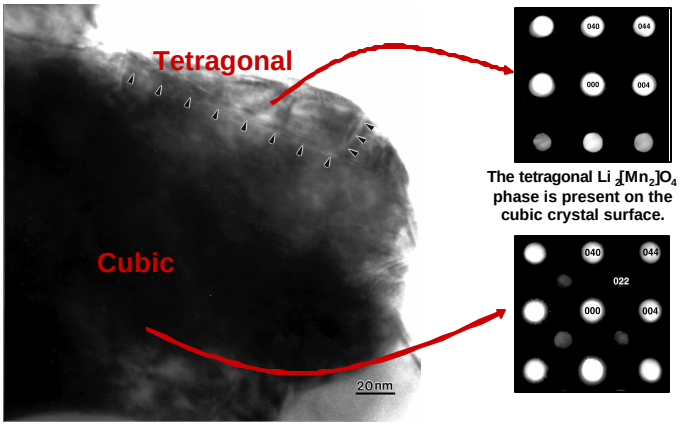

Figure 16.8 A transmission electron microscope image of a $Li_x[Mn_2]O_4$ crystal, extracted from a $Li/Li_x[Mn_2]O_4$ cell discharged to 3.3 V vs. lithium, showing a phase boundary near the surface of the crystal marked by arrows. The electron diffraction patterns collected from the surface and the center of the crystal using a 20 nm electron beam probe are shown on the right[40].

TEM data of a spinel $Li_x[Mn_2]O_4$ crystal, extracted from a $Li/Li_x[Mn_2]O_4$ cell discharged to 3.3 V vs. lithium, are presented in Figure 16.8..The dark fringes in the image marked by arrows are associated with the cubic and tetragonal phase boundary. The phase change across the boundary is confirmed by electron diffraction analysis of two regions. The diffraction pattern obtained from the crystal center (right bottom) has a four-fold symmetry, corresponding to the cubic phase. In contrast, the pattern from the crystal surface (right top) exhibits a two-fold symmetry, corresponding to the tetragonal phase. In addition, the absence of {220} reflections and the non-equivalence of the (040) and (004) reflections are consistent with tetragonal rock-salt $Li_2[Mn_2]O_4$. Therefore, TEM analysis has provided direct experimental evidence for localized, cubic to tetragonal transformation induced by the Jahn-Teller distortion of Mn^{3+} during cycling of 4V $Li/Li_x[Mn_2]O_4$ batteries. Substitution of monovalent, divalent and trivalent ions in $Li[M_xMn_{2-x}]O_4$ can increase the average valence state of Mn ions, suppress the cooperative Jahn-Teller distortion of Mn^{3+} ions and thus the cubic-tetragonal transition, and eventually improve the cycling performance of 4V $Li[M_xMn_{2-x}]O_4$ spinel electrodes[92]. Although TEM studies have revealed the formation of tetragonal $Li_2[Mn_2]O_4$, further research is still needed to correlate this phase transformation to capacity fading of $Li/Li_x[Mn_2]O_4$ cells during electrochemical cycling.

16.5. Phase Transformations Between 2D Layered And 3D Spinel-Related Configurations

The layered structure and the lithiated-spinel structures have close-packed oxygen arrays (which, in practice, usually deviate slightly from ideal cubic-close-packing) but differ in the arrangement of the transition metal and lithium ions. The layered $LiMO_2$ structure has one set of unique close-packed planes, i.e., the (001) planes, which is parallel to one of four equivalent close-packed planes of the lithiated-spinel $Li_2[M_2]O_4$ structure, i.e., the (111), $(\bar{1}11)$, $(1\bar{1}1)$ and $(\bar{1}\,\bar{1}1)$ planes. In the lithiated-spinel $Li_2[M_2]O_4$ structure, the transition metal ions are distributed between the alternate close-packed oxygen layers in a 3:1 ratio. Therefore, if one-quarter of the transition metal ions in the lithiated-spinel structure is transposed with one-quarter of the lithium ions, the lithiated-spinel structure is then transformed to the layered structure. An intermediate cation distribution occurs if these transition metal ions are partially transposed with the lithium ions. X-ray and neutron powder diffraction patterns of layered $LiMO_2$ and lithiated-spinel $Li_2[M_2]O_4$ structures (M = transition metal cation) often share strong resemblance, particularly when the *c/a* ratio approaches 4.899, which leads to ambiguity in identifying whether the cation configuration in lithium electrode

materials is 2D layered or 3D spinel-related. In the case of layered O3-$LiCoO_2$ with a *c/a* ratio of 4.99, it is reasonably easy to distinguish the layered structure. It is especially difficult to distinguish structures with cation distributions intermediate between those of the ideal layered and ideal spinel configurations by X-ray powder diffraction. Single-crystal electron diffraction analyses of individual crystals provide phase relationships among different atomic planes, which can determine whether the structure is layered or spinel-related. In addition, the electron scattering intensity can be used to quantify intermediate cation distributions in lithium transition metal oxides.

The lithiated-spinel structure can be converted to the layered structure if the four transition metal ions on the 16d sites with coordinates (¼, ½, ¼), (¼, 0, ¾), (¾, ½, ¾) and (¾, 0, ¼), are transposed with the four lithium atoms on the 16c sites with coordinates (¼, 0, ¼), (¼, ½, ¾), (¾, 0, ¾) and (¾, ½, ¼)[94]. An intermediate structure is produced when a fraction of these transition metal and lithium ions are transposed and such an intermediate structure can be determined quantitatively by examining and comparing the intensities of four sets of the {111} planes in the lithiated-spinel structure and the (003) planes in the layered structure.

The structure factor $F_{(003)}$ of the (003) atomic planes in the layered structure with space group symmetry $R\bar{3}m$ and with a cubic close-packed oxygen array and the oxygen ions located at (0, 0, 0.24) is given by:

$$F_{(003)} = 3(f_M - f_{Li}) + 1.124\ f_o \qquad (7)$$

Where f_M is the scattering factor of a transition metal ion, f_O is the scattering factor of an oxygen ion and f_{Li} is the scattering factor of a lithium ion. When considering an equivalent number of atoms in the layered structure to the number of atoms in one unit cell of the lithiated-spinel structure and ignoring the scattering of oxygen ($1.124f_O$ is significantly smaller than $3f_M$), then

$$F'_{(003)} = 16(f_M - f_{Li}) \qquad (8)$$

and the total scattering intensity of the (003) planes in the layered structure is

$$I'_{(003)} \propto 2(F'_{(003)})^2 = 512\ (f_M - f_{Li})^2 \qquad (9)$$

In the case of an ideal lithiated-spinel $Li_{16}[M_{16}]O_{32}$ structure with space group $Fd\bar{3}m$, the structure factor $F_{\{111\}}$ and the total scattering intensity $I_{\{111\}}$ for the {111} atomic planes have the following relationships (the scattering of oxygen is neglected):

$$F_{\{111\}} = 8(f_M - f_{Li}) \qquad (10)$$

$$I_{\{111\}} \propto 8(F_{\{111\}})^2 = 512\ (f_M - f_{Li})^2 \qquad (11)$$

These equations indicate that the total scattering intensity from the (003) reflections in the layered structure equals that from the {111} reflections of

the lithiated-spinel structure.

Now we consider intermediate cation distributions that deviate from the ideal lithiated-spinel and layered configurations, which can be described by the following formula: $\{(Li_{16-4x})_{16c}[Li_{4x}]_{16d}\}_{layer1}\{(M_{16-4x})_{16d}[M_{4x}]_{16c}\}_{layer2}O_{32}$ in spinel notation. When $x = 0$, the structure has the ideal lithiated-spinel configuration, $(Li_{16})_{16c}[M_{16}]_{16d}O_{32}$, or $(Li_2)_{16c}[M_2]_{16d}O_4$. When $x = 1$, it has the layered configuration, $\{(Li_{12})_{16c}[Li_4]_{16d}\}_{layer1}\{(M_{12})_{16d}[M_4]_{16c}\}_{layer2}O_{32}$ (alternatively, in the layered notation, $(Li_3)_{3a}[M_3]_{3b}O_6$). The magnitude of the structure factor and the scattering intensity for the set of the {111} planes with increasing transition metal density, *e.g.*, the $(1\,\bar{1}\,1)$ reflection can be described as a function of x:

$$F_{(1\bar{1}1)} = (8f_M + 8xf_M - 8f_{Li} - 8xf_{Li}) \qquad (12)$$

The magnitudes of the structure factors and the scattering intensities for each of the other three sets of the {111} planes with decreasing transition metal densities, can also be described as a function of x:

$$F_{(111)} = (8f_M - 8xf_M - 8f_{Li} + 8xf_{Li}) \qquad (13)$$

The ratio between the scattering intensities of the (111) and $(1\,\bar{1}\,1)$ planes, denoted as m, can be related to x by the following equation:

$$m = \frac{I_{(111)}}{I_{(1\bar{1}1)}} = \frac{(1-x)^2}{(1+x)^2} \qquad (14)$$

As shown in Figure 16.10., m decreases as x increases, *i.e.*, where the specific occupancies of lithium and transition metal ions in the structure vary from the lithiated-spinel to the layered configuration.

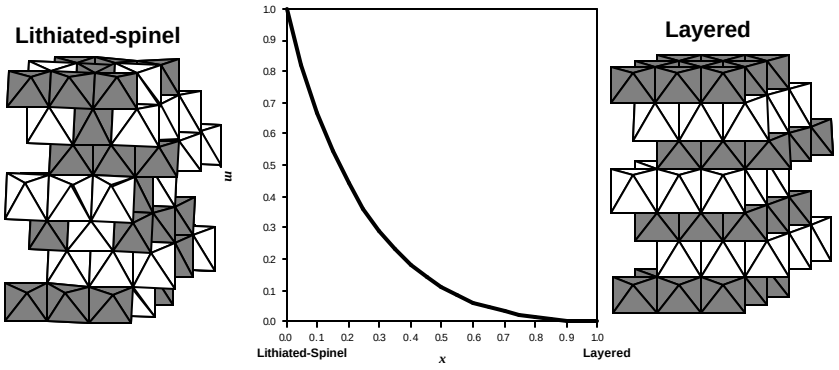

Figure 16.9. The scattering intensity ratio of the (111) and $(1\,\bar{1}\,1)$ planes, m, decreases as the cation distribution varies from the ideal lithiated-spinel to the ideal layered configuration[31].

One can determine the values of x, the degree of cation distribution

between the layered and the lithiated-spinel configurations, by measuring the relative intensity ratios of the {111} reflections. The caveat to this approach is that the dynamical diffraction conditions often encountered in transmission electron microscopy studies would tend to reduce the intensity differences among the {111} reflections. Taken together with the experimental fact that variations in the {111} scattering intensity are observed, it is apparent that the diffraction conditions of thin crystals with slight deviation from the exact zone axis are consistent with the kinematical approximation. This approach has proven particularly powerful in analyzing the structural features of LT-$LiCoO_2$ upon heat-treatments[31,35] and the structural stability of layered O3 Li_xMnO_2 during electrochemical cycling[21].

16.5.1. Intermediate Layered-Spinel Cation Configurations in LT-$LiCoO_2$

LT-$LiCoO_2$ synthesized at 400 ºC has been studied extensively as a positive electrode material for lithium batteries[95]. X-ray powder diffraction data and vibration spectroscopy studies have determined that LT-$LiCoO_2$ has the lithiated-spinel $Li_2[Co_2]O_4$ structure (space group $Fd3m$)[96,97]. LT-$LiCoO_2$ electrodes do not perform well in lithium cells, and there is considerable hysteresis between the lithium de-intercalation and intercalation processes, which contrasts with the superior electrochemical performance of electrodes with layered O3 $LiCoO_2$ structure (space group $R\bar{3}m$)[95]. In addition, the voltage profile of Li/LT-Li_xCoO_2 cells is considerably different from that of Li/$Li_x[Mn_2]O_4$ spinel cells, which calls into question the ideal lithiated-spinel cation configuration of LT-$LiCoO_2$. TEM analyses of LT-$LiCoO_2$ crystals have shown that the cobalt distribution in LT-$LiCoO_2$ samples is not ideal, and that it can be considered to be intermediate between an ideal layered $(Li)_{3a}\{Co\}_{3b}O_2$ configuration and an ideal lithiated-spinel $(Li_2)_{16c}[Co_2]_{16d}O_4$ configuration[31].

Crystal morphology of LT-$LiCoO_2$ crystals and two single-crystal electron diffraction patterns collected from two different LT-$LiCoO_2$ crystals are shown in Figure 16.10.. TEM imaging reveals that the average crystal size of LT-$LiCoO_2$ is on the order of 20 nm, which supports the use of the kinematical approximation in electron diffraction intensity analysis. Both diffraction patterns are indexed according to the lithiated-spinel structure with cubic symmetry (*Fd3m*) along the $[10\bar{1}]$ direction; they cannot be indexed consistently with trigonal symmetry ($R\bar{3}m$). The (111) and $(1\bar{1}1)$ reciprocal points in one pattern (top right of Figure 16.10.) have similar scattering intensities with an intensity ratio of 0.95, as expected for an ideal lithiated-spinel structure. In contrast, the (111) and $(1\bar{1}1)$ reflections in the other pattern (bottom left of Figure 16.10.) have significantly different scattering

intensities with an intensity ratio of 0.25. The scattering intensity variation observed in the {111} planes, which can be quantified digitally from the electron diffraction patterns, is then used to determine *x*, the parameter to describe non-ideal cation distribution intermediate between the layered and lithiated-spinel structures based on Equations 12-14 and Figure 16.9.. There are significantly more crystals that have a configuration closer to the lithiated-spinel structure ($x < 0.5$) than to the layered structure ($x > 0.5$) in LT-$LiCoO_2$, as shown in the bottom right graph of Figure 16.10.. These electron diffraction results not only confirm that the lithiated-spinel structure is the major phase in LT-$LiCoO_2$ products but also provide an explanation for the previously reported, poor electrochemical properties of LT-$LiCoO_2$ in lithium batteries. The mixing of cobalt and lithium ions in layered or lithiated-spinel $LiCoO_2$ structures will restrict the two-dimensional or three-dimensional pathways for lithium diffusion that are normally accessible in the ideal layered and ideal spinel structures, respectively. Therefore, the poor electrochemical behavior of Li/LT-$LiCoO_2$ cells can be attributed to the intermediate cation distribution between the layered and the lithiated-spinel structures in LT-$LiCoO_2$.

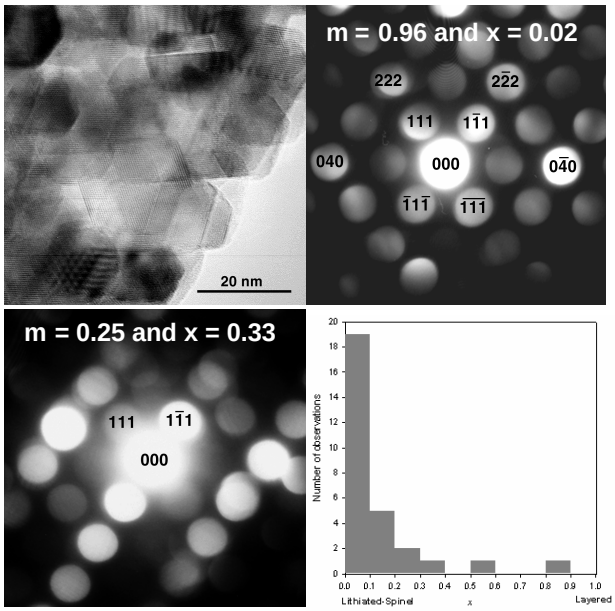

Figure 16.10. A high-resolution TEM image (top left) of LT-$LiCoO_2$ crystals showing the average crystal size on the order of 20 nm, and two single-crystal electron diffraction patterns with dissimilar scattering intensity ratios of the (111) and (1 $\bar{1}$ 1) planes[31]. The number of crystals analyzed in the LT-$LiCoO_2$ sample is plotted as a function of x (bottom right).

16.5.2. Layered to Spinel Transformation in Cycled Li_xMnO_2

Extensive research efforts have been focused on developing layered O3 $LiMnO_2$, isostructural to layered O3 $LiCoO_2$ in order to reduce the cost and improve the safety aspects of positive electrode materials in lithium batteries[9,11]. The voltage profile of Li/Li_xMnO_2 cells is modified considerably upon the first intercalation process and subsequent voltage profiles of cycled Li/Li_xMnO_2 cells resemble those of the layered and the spinel compounds[21]. It is believed that some Mn ions in the MnO_2 slabs migrate into the lithium plane during lithium de-intercalation, resulting in localized, spinel-type cation arrangements. However, similarities between the X-ray powder diffraction patterns of the lithium-spinel $Li_2[Mn_2]O_4$ and layered Li_xMnO_2 phases lead to ambiguities in understanding phase transformations underwent in Li_xMnO_2 electrodes, which prevents confirmation of the spinel-type configuration with certainty. The combination of high-resolution lattice imaging and electron diffraction[21] has revealed the formation of localized, spinel domains in the cycled Li_xMnO_2.

A typical high resolution TEM image and the corresponding electron diffraction pattern of one as-prepared $LiMnO_2$ crystal and a randomly selected crystal in the $Li_{0.5}MnO_2$ electrode obtained after one charge and one partial discharge are compared in Figure 16.12.. It should be pointed out that two sets of lattice fringes and the corresponding reflections (right of Figure 16.11.) indicate the presence of two sets of close-packed planes in the Li_xMnO_2 structure in contrast to one allowed in the layered $LiMnO_2$ structure (left of Figure 16.11.). The occurrence of more than one set of close-packed Mn planes corresponds to the presence of the spinel-type configuration. As some manganese ions have migrated into lithium planes during lithium de-intercalation and are trapped in the lithium layers upon lithium re-intercalation, localized cation distributions resemble that of the spinel. In addition, it can be argued that the non-equivalent scattering intensity of the {111} reflections of the spinel-type structure in the Li_xMnO_2 sample can be attributed to a non-uniform cation distribution within individual Li_xMnO_2 crystals with discrete domains, where each domain has a cation distribution of either the layered or the spinel-type configuration. The averaged cation distribution over each crystal can be regarded as being intermediate between that of the layered and the lithiated-spinel structures, which can be quantified according to Equation 12-14 and Figure 16.9.. Therefore, the combination of high-resolution TEM imaging and electron diffraction has clearly revealed the structural instability of the layered Li_xMnO_2 structure and provided direct evidence of spinel-type atomic arrangements in cycled Li_xMnO_2 electrode materials. Furthermore, Chiang *et al.*[46] have proposed the formation of antiphase boundaries upon transformation from layered $LiMnO_2$ to the spinel configuration during electrochemical cycling. Further high-resolution TEM

imaging and theoretical calculations are needed to verify the presence and the energetics of nanometer-scale antiphase domains in lithium transition metal oxides.

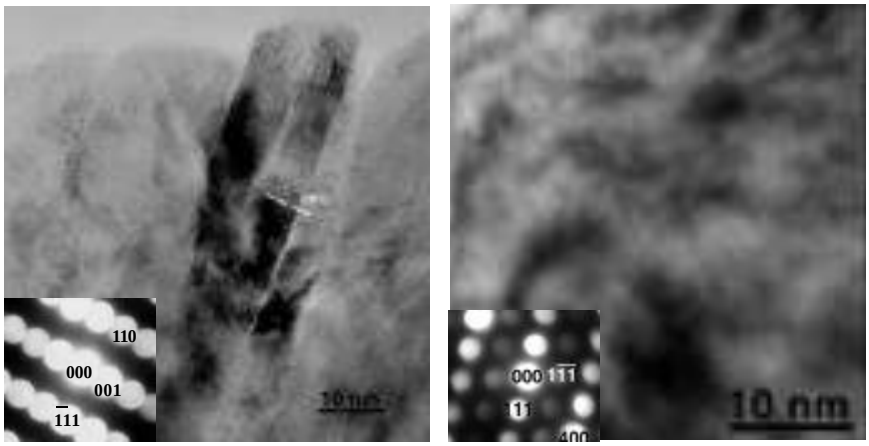

Figure 16.11. Left: A typical high-resolution TEM micrograph and the corresponding electron diffraction pattern $\{[1\,\bar{1}\,0]_{layered}$ zone axis$\}$ of layered $LiMnO_2$ crystals and Right: A high-resolution TEM image and the corresponding electron diffraction pattern $\{[0\,\bar{1}\,1]_{spinel}$ zone axis$\}$ of a randomly selected crystal in the $Li_{0.5}MnO_2$ electrode after one charge and one partial discharge[21].

16.6. PERSPECTIVES

Conventional TEM imaging and electron diffraction studies of lithium battery materials have been invaluable in revealing phase transformations that occur in lithium battery materials during lithium de-intercalation or intercalation. The information has led to improved understanding of structure-property relationships of lithium intercalation compounds and optimization of battery performance through design of new electrode materials. Here we discuss several recently developed TEM techniques that can be used to further improve our fundamental understanding of lithium intercalation compounds in lithium batteries.

16.6.1. High-Resolution TEM Imaging and Simulation

Although X-ray and neutron powder diffraction techniques are insensitive to lithium ion arrangements, columns of lithium in host structures can potentially be imaged (along with the columns of other atoms present) by making use of their interactions with an electron beam in the high-resolution TEM (HRTEM). The results of the electrons' interaction with the lithium

transition metal oxide lattice are encoded on the emergent electron wave as changes in the phase (and, to a lesser extent, the amplitude) of the original incident electron wave. The phase of this exit-surface wave (ESW) is a function of the oxide potential projected in the direction of the incident electron beam[98]. In the HRTEM, the ESW phase is imaged with an objective lens that imposes additional phase changes due to aberrations such as defect of focus (defocus) and spherical aberration. Focal-series reconstruction (FSR) of the ESW from a series of images obtained over a range of defocus values[99] can mitigate the effects of spherical aberration, and move beyond the native resolution of a TEM to its information limit[98]. This method has achieved resolution of oxygen atoms in staurolite[100] and $BaTiO_3$[101], and recently it has been used to successfully image and resolve individual lithium ions in layered O3 $LiCoO_2$.

As shown in Figure 16.13., image simulation via the "weak-phase-object" approximation indicates that resolutions higher than 1 Å are needed to resolve individual lithium ions in layered CoO_2 matrix[39]. The ESW phase image reconstructed from experimental images of a thin edge of a $LiCoO_2$ crystal along the [110] zone axis shows all three types of atoms in $LiCoO_2$ (Figure 16.13., right a)[39]. Comparison with a simulated ESW phase image based on a crystal model of 17 unit cells thick (48 Å) at 0.9 Å resolution (Figure 16.13., right b), reveals that all the atom peaks have the characteristics predicted by the simulations. The O-Co-O units can clearly be distinguished in the experimental image, with each fuzzy cobalt peak flanked by a pair of bright oxygen atoms, and the weak spots lying between them can be identified as the electron scattering intensities of the lithium ions (arrowed).

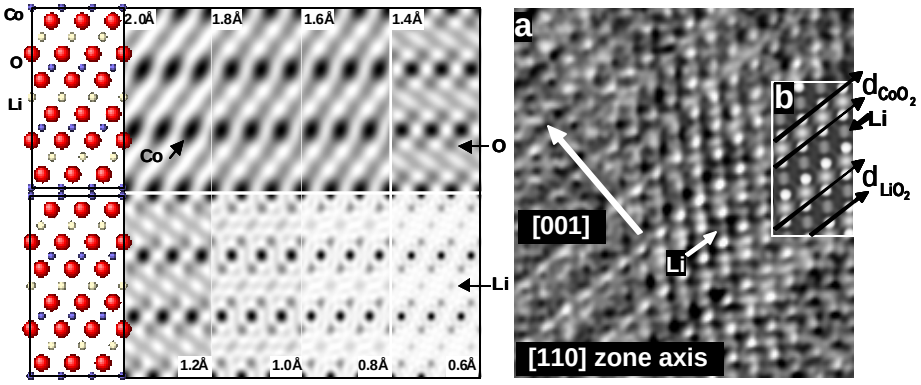

Figure 16.13. Left: Simulated Images of $LiCoO_2$ in the [110] zone axis under thin-crystal ("weak-phase-object") conditions for increasing resolution (marked) show that atoms of cobalt should be visible at 2 Å resolution, oxygen at 1.4 Å, and lithium at 1 Å. Right: Experimental imaging of Li columns confirmed by simulation a) $LiCoO_2$ ESW-phase image, reconstructed from 20 experimental images, shows lithium ions in rows (arrowed) between O-Co-O groups. b) ESW-phase simulation for 48 Å thickness and 0.9 Å resolution[39].

Studies with such atomic details can provide knowledge of the distribution of vacancies and light atoms such as lithium and oxygen in lithium transition metal oxides, which is invaluable to engineering of lithium storage materials.

16.6.2. EELS Analysis and Imaging

Much attention has been focused on characterizing localized atomic arrangements and phase transformations by electron diffraction and imaging techniques. It is also important to analyze the chemical and electronic properties of lithium battery materials upon lithium intercalation or de-intercalation. Although high-resolution images are sensitive to differences in structural factors, the combined effect of differences in structural factors and deviation from the exact Bragg condition leads to ambiguity in revealing differences in local chemical compositions from TEM images. EELS could provide quantitative information on light elements such as lithium and oxygen, and determine the valence states of transition metal and oxygen ions in lithium transition metal oxides. Recently Graetz et al.[49,51] have used EELS analyses to study and confirm charge compensation mechanisms in layered Li_xCoO_2 and $Li_xNi_{0.8}Co_{0.2}O_2$ upon lithium de-intercalation, which has been previously predicted from first-principle studies[60,78]. In addition, imaging with EELS can provide information about how different ions are distributed in lithium transition metal oxides on the nanometer-scale. Combined information on the chemistry, structure and electronic properties of localized domains in lithium battery materials will enable us to optimize and advance lithium battery performance.

16.6.3. In-Situ TEM imaging

One way that offers the possibility of overcoming material stability and handling limitations of TEM sample preparation is to develop *in-situ* TEM characterization and observe the phase transformations in electrode materials in an electrochemical cell *in-situ*. The *in-situ* cell could be built containing solid or liquid electrolytes. The difficulties in design of *in-situ* electrochemical cells reside in the facts that the whole cell has to be thin enough to be electron transparent and hermetically sealed. Ross recently reported a preliminary design of a liquid *in-situ* cell to study the electroplating process, which is a critical step in integrated circuit fabrication[102]. Although it was found too thick to be electron transparent, it held promise for real-time studies of electrochemical systems. More importantly, *in-situ* characterization would offer an effective route to study many interfacial phenomena between the electrode and electrolyte, and provide directions to improve the safety and

storage aspects of battery systems. Interfacial reactions may include the formation of the solid electrolyte interface on the negative and/or positive electrode before electrochemical reactions, the chemical stability of electrode materials at the electrolyte-electrode interface during electrochemical reactions and storage, *etc*. At present, these interfacial reactions are not well studied nor clearly understood. Observations *in-situ* before, during and after electrochemical reactions would provide information essential to better understanding of these phenomena.

Acknowledgments

The author is grateful to A. Mayes, G. Ceder, A. Van der Ven and C. Delmas for comments and insightful discussions. The International Research Fellow Award INT 0000-429 from National Science Foundation and partial support from Department of Mechanical Engineering at the Massachusetts Institute of Technology and Office of Naval Research Young Investigator Award N00014-03-10448 are greatly acknowledged.

References

1. D. Linden & T. Reddy (eds.) *Handbook of Batteries* (McGraw-Hill, New York, 2002).
2. K. Mizushima, P. C. Jones, P. J. Wiseman & J. B. Goodenough, *Materials Research Bulletin* **15**, 783-789 (1980).
3. J. N. Reimers & J. R. Dahn, *J. Electrochem. Soc.* **139**, 2091-2097 (1992).
4. T. Ohzuku & A. Ueda, *J. Electrochem. Soc.* **141**, 2972-2977 (1994).
5. J. Morales, C. Pérez-Vicente & J. L. Tirado, *Materials Research Bulletin* **25**, 623-630 (1990).
6. J. R. Dahn, U. Von Sacken, M. W. Juzkow & H. Al-Janaby, *J. Electrochem. Soc.* **138**, 2207-2211 (1991).
7. M. Broussely, F. Perton, P. Biensan, J. M. Bodet, J. Labat, A. Lecerf, C. Delmas, A. Rougier & J. P. Pérès, *Journal of Power Sources* **54**, 109-114 (1995).
8. C. Delmas, M. Ménétrier, L. Croguennec, I. Saadoune, A. Rougier, C. Pouillerie, G. Prado, M. Grüne & L. Fournès, *Electrochimica Acta* **45**, 243-253 (1999).
9. A. R. Armstrong & P. G. Bruce, *Nature* **381**, 499-500 (1996).
10. P. G. Bruce, A. R. Armstrong & H. Huang, *Journal of Power Sources* **68**, 19-23 (1997).
11. F. Capitaine, P. Gravereau & C. Delmas, *Solid State Ionics* **89**, 197 (1996).
12. M. M. Thackeray, P. J. Johnson, L. A. De Picciotto, P. G. Bruce & J. B. Goodenough, *Materials Research Bulletin* **19**, 179 (1984).
13. W. I. F. David, M. M. Thackeray, L. A. De Picciotto & J. B. Goodenough, *Journal of Solid State Chemistry* **67**, 316-323 (1987).
14. M. M. Thackeray, W. I. F. David, P. G. Bruce & J. B. Goodenough, *Materials Research Bulletin* **18**, 461 (1983).
15. A. K. Padhi, K. S. Nanjundaswamy & J. B. Goodenough, *Journal of the Electrochemical Society* **144**, 1188 (1997).
16. J.-M. Tarascon & M. Armand, *Nature* **414**, 359 (2001).
17. M. M. Thackeray, J. O. Thomas & M. S. Whittingham, *MRS Bulletin*, 39 (2000).
18. C. Delmas, J. P. Pérès, A. Rougier, A. Demourgues, F. Weill, A. Chadwick, M. Broussely, F. Perton, P. Biensan & P. Willmann, *Journal of Power Sources* **68**, 120-125 (1997).
19. M. Ménétrier, I. Saadoune, S. Levasseur & C. Delmas, *Journal of Materials Chemistry* **9**, 1135-1140 (1999).
20. G. Vitins & K. West, *Journal of the Electrochemical Society* **144**, 2587-2592 (1997).
21. Y. Shao-Horn, S. A. Hackney, A. R. Armstrong, P. G. Bruce, R. Gitzendanner, C. S. Johnson & M. M. Thackeray, *J. Electrochem. Soc.* **146**, 2404-2412 (1999).
22. H. F. Wang, Y. I. Jang & Y. M. Chiang, *Electrochemical and Solid State Letters* **2**, 490-493 (1999).
23. J. Rodriguez-Carjaval, G. Rousse, C. Masquelier & M. Hervieux, *Physical Review Letters* **81**, 4660 (1998).
24. G. Rousse, C. Masquelier, J. Rodriguez-Carjajal & M. Hervieu, *Electrochemical and Solid-State Letters* **2**, 6-8 (1999).
25. G. Rousse, C. Masquelier, J. Rodriguezcarvajal, E. Elkaim, J. P. Lauriat & J. L. Martinez, *Chemistry of Materials* **11**, 3629-3635 (1999).
26. A. J. Garcia-Adeva, D. R. Conradson, P. Villella & S. D. Conradson, *J. Phys. Chem. B, 107 (28), , 2003* **107**, 6704 -6716 (2003).
27. P. Hirsch, A. Howie, R. Nicholson, D. W. Pashley & M. J. Whelan. *Electron Microscopy of Thin Crystals* (Krieger Publishing Company, 1977).
28. D. B. Williams & C. B. Carter. *Transmission Electron Microscopy - A Textbook for Materials Science* (Plenum Press, New York, 1996).
29. B. Fultz & J. M. Howe. *Transmission Electron Microscopy and Diffractometry of Materials* (Springer, Berlin, 2002).

30. P. R. Buseck, J. M. Cowley & L. Eyring (eds.) *High-Resolution Transmission Electron Microscopy and Associated Techniques* (Oxford Science Publications, 1992).
31. Y. Shao-Horn, S. A. Hackney, C. S. Johnson, A. J. Kahaian & M. M. Tackeray, *Journal of Solid State Chemistry* **140**, 116-127 (1998).
32. Y. Shao-Horn, S. A. Hackney, C. S. Johnson & M. M. Thackeray, *J. Electrochem. Soc.* **145**, 582-589 (1998).
33. Y. Shao-Horn, Ph.D dissertation, Michigan Technological University, Houghton, Michigan, USA (1998).
34. Y. Shao-Horn, S. A. Hackney, A. J. Kahaian, K. D. Kepler, E. Skinner, J. T. Vaughey & M. M. Thackeray, *Journal of Power Sources* **81-82**, 496 (1999).
35. Y. Shao-Horn, S. A. Hackney, A. J. Kahaian & M. M. Thackeray, *Journal of Solid State Chemistry* **168**, 60 (2002).
36. Y. Shao-Horn, M. A. O'Keefe, E. C. Nelson, L. Croguennec & C. Delmas. in *Fall Meeting of the Materials Research Society, Symposium G, Boston, Massachusetts* (2002).
37. Y. Shao-Horn, S. Levasseur, F. Weill & C. Delmas, *J. Electrochem. Soc.* **150**, A366-A373 (2003).
38. Y. Shao-Horn, L. Croguennec, D. Carlier, F. Weill, M. Menetrier & C. Delmas, *Chemistry of Materials* **15**, 2977-2983 (2003).
39. Y. Shao-Horn, L. Croguennec, C. Delmas, E. C. Nelson & M. A. O'Keefe, *Nature Materials* **2**, 464-467 (2003).
40. M. M. Thackeray, Y. Shao-Horn, A. J. Kahaian, K. D. Kepler, E. Skinner, J. T. Vaughey & S. A. Hackney, *Electrochemical and Solid-State Letters* **1**, 7-9 (1998).
41. M. M. Thackeray, C. S. Johnson, Kahaian, A.J., K. D. Kepler, J. T. Vaughey, Y. Shao-Horn & S. A. Hackney, *J. Power Sources* **81-82**, 60 (1999).
42. J. P. Pérès, F. Weill & C. Delmas, *Solid State Ionics* **116**, 19 (1999).
43. H. Wang, Y. I. Jang, B. Huang, D. R. Sadoway & Y. M. Chiang. in *9th International Symposium on Intercalation Compounds* abstract N°111 (Molecular Crystals and Liquid Crystals Science and Technology, Arcachon (FRANCE), 1998).
44. H. F. Wang, Y. I. Jang, B. Y. Huang, D. R. Sadoway & Y. T. Chiang, *J. Electrochem. Soc.* **146**, 473-480 (1999).
45. H. F. Wang, Y. I. Jang, B. Y. Huang, D. R. Sadoway & Y. M. Chiang, *Journal of Power Sources* **82**, 594-598 (1999).
46. Y. Chiang, H. F. Wang & Y. I. Jang, *Chemistry of Materials* **13**, 53-63 (2001).
47. Gabrisch H., R. Yazami & B. Fultz, *Electrochemical and Solid State Letters* **5**, A111 (2002).
48. L. Croguennec, P. Deniard, R. Brec, M. T. Caldes Ricos & L. Brohan, *Mol. Cryst. Liq. Cryst.* **311**, 101-108 (1998).
49. J. Graetz, C. C. Ahn, R. Yazami & B. Fultz, *Journal of Physical Chemistry B* **107**, 2887-2891 (2003).
50. H. Gabrisch, R. Yazami & B. Fultz, *Electrochemical and Solid State Letters* **5**, A111-A114 (2002).
51. J. Graetz, A. Hightower, C. C. Ahn, R. Yazami, P. Rez & B. Fultz, *Journal of Physical Chemistry B* **106**, 1286-1289 (2002).
52. A. Hightower, C. C. Ahn, B. Fultz & P. Rez, *Applied Physics Letters* **77**, 238-240 (2000).
53. Y. Shao-Horn, L. Croguennec, A. Gloter, M. Guilmard, C. Colliex & C. Delmas, *Chemistry of Materials*, submitted (2003).
54. A. H. Thompson, *Physical Review Letters* **40**, 1511-1514 (1978).
55. W. R. McKinnon & J. R. Dahn, *Solid State Communications* **48**, 43-45 (1983).
56. C. Delmas, M. Ménétrier, L. Croguennec, S. Levasseur, J. P. Pérès, C. Pouillerie, G. Prado, L. Fournès & F. Weill, *Inter. J. of Inorg. Mater.* **1**, 11 (1999).
57. A. Van der Ven & G. Ceder, *Electrochemical and Solid State Letters* **3**, 301-304 (2000).
58. M. Catti, *Physical Review B* **61**, 1795-1803 (2000).
59. C. Wolverton & A. Zunger, *Physical Review B - Condensed Matter* **57**, 2242-2252 (1998).

60. C. Wolverton & A. Zunger, *Physical Review Letters* **81**, 606-609 (1998).
61. C. Wolverton & A. Zunger, *Journal of Power Sources* **82**, 680-684 (1999).
62. D. Carlier, A. Van der Ven, C. Delmas & G. Ceder, *Chemistry of Materials* **15**, 2651-2660 (2003).
63. M. de Dompablo, A. Van der Ven & G. Ceder, *Physical Review B* **66**, art. no.-064112 (2002).
64. M. E. Arroyo y de Dompablo & G. Ceder, *Chemistry of Materials* **15**, 63-67 (2003).
65. I. Saadoune & C. Delmas, *Journal of Solid State Chemistry* **136**, 8-15 (1998).
66. S. Levasseur, M. Menetrier, E. Suard & C. Delmas, *Solid State Ionics* **128**, 11-24 (2000).
67. W. Li, J. N. Reimers & J. R. Dahn, *Solid State Ionics* **67**, 123-130 (1993).
68. T. Ohzuku, A. Ueda & M. Nagayama, *J. Electrochem. Soc.* **140**, 1862-1870 (1993).
69. A. Hirano, R. Kanno, Y. Kawamoto, Y. Takeda, K. Yamaura, M. Takano, K. Ohyama, M. Ohashi & Y. Yamaguchi, *Solid State Ionics* **78**, 123-131 (1995).
70. M. G. S. R. Thomas, P. G. Bruce & J. B. Goodenough, *Solid State Ionics* **17**, 13-19 (1985).
71. S. Kikkawa, S. Miyazaki & M. Koizumi, *Journal of Solid State Chemistry* **62**, 35 (1986).
72. E. Plichta, M. Salomon, S. Slane, M. Uchiyama, D. Chua, W. B. Ebner & H. W. Lin, *Journal of Power Sources* **21**, 25-31 (1987).
73. J. Molenda, A. Stoklosa & T. Bak, *Solid State Ionics* **36**, 53-58 (1989).
74. J. P. Kemp & P. A. Cox, *J. Phys.: Condens. Matter* **2**, 9653-9667 (1990).
75. G. G. Amatucci, J. M. Tarascon & L. C. Klein, *J. Electrochem. Soc.* **143**, 1114-1123 (1996).
76. M. K. Aydinol, A. F. Kohan & G. Ceder, *Journal of Power Sources* **68**, 664-668 (1997).
77. A. Van der Ven, M. K. Aydinol & G. Ceder, *J. Electrochem. Soc.* **145**, 2149-2155 (1998).
78. A. Van der Ven, M. K. Aydinol, G. Ceder, G. Kresse & J. Hafner, *Physical Review B* **58**, 2975-2987 (1998).
79. C. Delmas, J. J. Braconnier & P. Hagenmuller, *Materials Research Bulletin* **17**, 117 (1982).
80. R. Siegel, J. Hirschinger, D. Carlier, S. Matar, M. Ménétrier & C. Delmas, *J Phys. Chem. B* **105**, 4166 (2001).
81. D. Carlier, I. Saadoune, E. Suard, L. Croguennec, M. Ménétrier & C. Delmas, *Solid State Ionics* **144**, 263 (2001).
82. D. Carlier, I. Saadoune, M. Ménétrier & C. Delmas, *J. Electrochem. Soc.* **149**, A1310 (2002).
83. J. M. Paulsen, C. L. Thomas & J. R. Dahn, *J. Electrochem. Soc.* **147**, 861 (2000).
84. J. M. Paulsen & J. R. Dahn, *J. Electrochem. Soc.* **147**, 2478 (2000).
85. J. M. Paulsen, C. L. Thomas & J. R. Dahn, *J. Electrochem. Soc.* **147**, 2862 (2000).
86. J. M. Paulsen, J. R. Mueller-Neuhaus & J. R. Dahn, *J. Electrochem. Soc.* **147**, 508 (2000).
87. J. M. Paulsen, R. A. Donaberger & J. R. Dahn, *Chem. Mater.* **12**, 2257 (2000).
88. Z. Lu & J. R. Dahn, *J. Electrochem. Soc.* **148**, A710 (2001).
89. Z. Lu & J. R. Dahn, *J. Electrochem. Soc.* **148**, A237 (2001).
90. A. Mendiboure, C. Delmas & P. Hagenmuller, *Materials Research Bulletin* **19**, 1383 (1984).
91. L. Dupont, M. Hervieu, G. Rousse, C. Masquelier, M. R. Palacin, Y. Chabre & J. M. Tarascon, *Journal of Solid State Chemistry* **155**, 394 (2000).
92. R. J. Gummow, A. De Kock & M. M. Thackeray, *Solid State Ionics* **69**, 59-67 (1994).
93. J.-M. Tarascon, E. Wang, F. K. Shokoohi, W. R. McKinnon & S. Colson, *Journal of the Electrochemical Society*, 2859 (1991).
94. R. J. Gummow, Ph.D dissertation, University of Cape Town (1993).
95. R. J. Gummow, M. M. Thackeray, D. Wif & S. Hull, *Materials Research Bulletin* **27**, 327-337 (1992).
96. W. Li, J. N. Reimers & J. R. Dahn, *Physical Review* **B 49**, 826 (1994).
97. W. Huang & R. Frech, *Solid State Ionics* **86-88**, 395-400 (1996).
98. M. A. O'Keefe, *Ultramicroscopy* **47**, 282-297 (1992).

99. P. Schiske. in *Image Processing And Computer-Aided Design* (ed. Hawkes, P. W.) 82-90 (Acad. Press, London, 1973).
100. K. H. Downing, M. Hu, H. Wenk & M. A. O'Keefe, *Nature* **348**, 525-528 (1990).
101. C. L. Jia & A. Thust, *Phys. Rev. Letts* **82**, 5052-5055 (1999).
102. F. M. Ross, *IBM J. Res. Develop.* **44**, 489 (2000).